JOURNAL OF THERMOPHYSICS AND HEAT TRANSFER
Vol. 7, No. 4, Oct.–Dec. 1993

Theory of Plume Radiance from the Bow Shock Ultraviolet 2 Rocket Flight

Graham V. Candler*
University of Minnesota, Minneapolis, Minnesota 55455
Deborah A. Levin†
Institute for Defense Analyses, Alexandria, Virginia 22311
Robert J. Collins‡
University of Minnesota, Minneapolis, Minnesota 55455
Peter W. Erdman§ and Edward Zipf¶
University of Pittsburgh, Pittsburgh, Pennsylvania 15260
and
Carl Howlett**
Utah State University, Logan, Utah 84322

A computational fluid dynamics algorithm is used to simulate the flowfield and solid rocket motor plume about the bow shock ultraviolet 2 flight vehicle. A new computationally efficient algorithm to model two-phase gas and particulate flow is developed. The flow over the complete rocket geometry and its interaction with the particle-laden plume is simulated. The computed plume radiance is compared with radiometric and spectroscopic data and good agreement with radiance magnitudes and spectral characteristics is obtained for the intrinsic core rocket exhaust data. The computation underpredicts the observed signal from the far-field photometers by many orders of magnitude. Based on the particulate flow simulations developed here and new experimental data, we hypothesize that the far-field radiation is due to molecular emission. Use of the CO Cameron band spectra obtained on this flight provides an estimate of the governing temperature of such radiation.

Introduction

THE bow shock ultraviolet 2 rocket experiment was flown in February 1991. This vehicle was instrumented to measure the radiation produced by the solid rocket motors during the flight at high altitudes. In this article, we develop and use a numerical method to simulate this flowfield and predict its radiative emission. The computed results are compared to those obtained from the experiment.

During data taking, the experimental flight vehicle underwent two solid rocket motor burns. During the first burn of interest, an Antares II motor fired, it was jettisoned, and then a Star-27 motor fired. The vehicle geometry during the Antares II burn is shown in Fig. 1. It is basically a 10.16-cm radius sphere −8.3-deg cone-cylinder configuration with a base radius of 39 cm and a length of 5.87 m. Periscopes were deployed to obtain optical measurements of the exhaust plume core and far field. These instruments viewed the flow at angles of 4 and 25 deg measured with respect to the centerline. At the 4-deg viewing angle a scanning spectrometer took spectrally-resolved data, and at both viewing angles a photometer centered at 230 nm with a bandwidth of 51 nm measured the radiance from the flowfield. Further details of the experimental configuration and additional measurements obtained are available in a companion article.[1]

It is the purpose of this article to develop and test a model for the simulation of solid rocket plumes. This model uses newly developed computational fluid dynamics (CFD) algorithms to obtain steady-state results with a reasonable computational cost. The plume/flowfield model treats the gas phase as composed of either air or nozzle exit gas, depending on its origin. The particulate phase is modeled using five different particle size bins. Separate mass, momentum, and energy conservation equations are solved for each bin, thus allowing different distributions of the particles at each location in the flow. The gas and the particles interact according to finite-rate momentum and energy exchange models; the results depend on the fidelity of these models. This model is used to compute the flowfield about the body at four different times during the flight. The radiative signal produced by the particles in the simulated flow is calculated and compared to the experimental results. The computed signal depends critically on the enthalpy assumed for the particles as they leave the motor nozzle.[2]

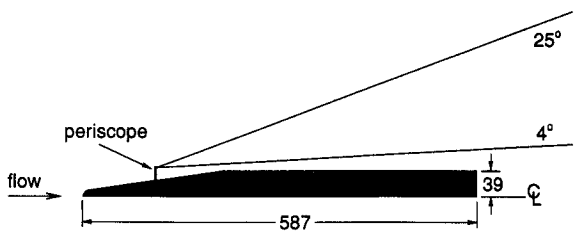

Fig. 1 Schematic of experimental configuration during the Antares II motor burn. Dimensions in cm. The rocket is 310 cm in length during the Star-27 burn.

Presented as Paper 92-0125 at the AIAA 30th Aerospace Sciences Meeting and Exhibit, Reno, NV, Jan. 6–9, 1992; received Sept. 23, 1992; revision received Jan. 28, 1993; accepted for publication Jan. 29, 1993.

*Assistant Professor, Department of Aerospace Engineering and Mechanics. Member AIAA.
†Research Staff Member, Science and Technology Division. Member AIAA.
‡Professor, Department of Electrical Engineering.
§Research Associate Professor, Department of Physics and Astronomy. Member AIAA.
¶Professor, Department of Physics and Astronomy. Member AIAA.
**Technical Program Manager, Center for Space Engineering. Member AIAA.

Plume Flowfield Modeling

The plume flowfield is modeled using two phases: 1) a gas phase and 2) a particle phase. The particulates are produced in the nozzle of the solid rocket and are allowed to interact with the gas that is produced by the rocket motor and the gas that originates in the freestream. In this section the governing equations that describe this flow are discussed and the assumptions that are implicit in the formulation are noted.

In a two-phase flow, the gas and particle phases may have different velocity fields and temperature distributions. Thus, we need to solve separate momentum and energy conservation equations for each phase. Additionally, if there is more than one size of particle in the flow, then the particulates may have different velocities and temperatures. In this case, we must solve momentum and energy conservation equations for each particle size. Thus, we take the approach of allowing there to be a prescribed set of discrete particle size bins into which we place the particulates that exit the rocket nozzle. The particle sizes are assumed to remain constant.

The governing equations for the gas are simply the axisymmetric Navier-Stokes equations with a source term to account for the interaction of the gas and particle phases. However, the gas that leaves the nozzle has different characteristics than the gas that originates in the freestream. Therefore, we must allow there to be two gas species present, but it is assumed that they do not react with one another. We can write the governing equations as

$$\frac{\partial \boldsymbol{U}}{\partial t} + \frac{\partial \boldsymbol{F}}{\partial x} + \frac{1}{y}\frac{\partial y\boldsymbol{G}}{\partial y} = \boldsymbol{W} \tag{1}$$

where $\boldsymbol{U}$ is the vector of conserved quantities, and $\boldsymbol{F}$ and $\boldsymbol{G}$ are the flux vectors in the axial, x, and radial, y directions. $\boldsymbol{W}$ is the source vector for the gas phase. These vectors are given by

$$\boldsymbol{U} = \begin{bmatrix} \rho_1 \\ \rho_2 \\ \rho u \\ \rho v \\ E \end{bmatrix} \qquad \boldsymbol{W} = \begin{bmatrix} 0 \\ 0 \\ w_{\rho u} \\ w_{\rho v} + [(1/y)(p + \tau_{\theta\theta})] \\ w_E \end{bmatrix}$$

$$\boldsymbol{F} = \begin{bmatrix} \rho_1 u + \rho_1 \tilde{u}_1 \\ \rho_2 u + \rho_2 \tilde{u}_2 \\ \rho u^2 + p + \tau_{xx} \\ \rho uv + \tau_{xy} \\ (E + p + \tau_{xx})u + \tau_{xy} v + q_x + \sum_s \rho_s h_s \tilde{u}_s \end{bmatrix} \tag{2}$$

$$\boldsymbol{G} = \begin{bmatrix} \rho_1 v + \rho_1 \tilde{v}_1 \\ \rho_2 v + \rho_2 \tilde{v}_2 \\ \rho uv + \tau_{xy} \\ \rho v^2 + p + \tau_{yy} \\ (E + p + \tau_{yy})v + \tau_{xy} u + q_y + \sum_s \rho_s h_s \tilde{v}_s \end{bmatrix}$$

where ρ_1 and ρ_2 are the densities of gas types 1 and 2. u and v are the mass-averaged velocities in the x and y directions, and $\tilde{u}_s$ and $\tilde{v}_s$ are the diffusion velocities of species s. The gas temperature and pressure may be found using the equations of state

$$E = \sum_{s=1}^{2} \rho_s c_{vs} T + \frac{1}{2}\rho(u^2 + v^2), \qquad p = \sum_{s=1}^{2} \rho_s \frac{R}{M_s} T \tag{3}$$

where c_{vs} and M_s are the specific heat and atomic weight of species s, respectively, and R is the universal gas constant. We have assumed that the specific heats do not change with temperature and that the gases do not react. The viscous terms are evaluated using Fickian diffusion with a constant Lewis number of 1.4 and linear stress-strain and temperature gradient-heat flux relationships. No-slip wall boundary conditions were used. This treatment of the viscous terms is not accurate at the high-altitude conditions of interest here, but it is felt that these inaccuracies have little effect on the radiation results. This will be discussed further in light of the computational results.

The governing equations for one size bin of the particle phase flow are essentially the same except that the viscous terms and the contribution of the pressure are absent. Thus, we have Eq. (1), except that the vectors are given by

$$\boldsymbol{U}_p = \begin{bmatrix} \rho_p \\ \rho_p u_p \\ \rho_p v_p \\ E_p \end{bmatrix} \qquad \boldsymbol{F}_p = \begin{bmatrix} \rho_p u_p \\ \rho_p u_p^2 \\ \rho_p u_p v_p \\ E_p u_p \end{bmatrix}$$

$$\boldsymbol{G}_p = \begin{bmatrix} \rho_p v_p \\ \rho_p u_p v_p \\ \rho_p v_p^2 \\ E_p v_p \end{bmatrix} \qquad \boldsymbol{W}_p = \begin{bmatrix} 0 \\ w_{\rho u_p} \\ w_{\rho v_p} \\ w_{E_p} \end{bmatrix} \tag{4}$$

where ρ_p is the density of the particles. u_p and v_p are the x and y particle velocities, and E_p is the particle energy per unit volume. The pressure and viscous terms are absent because it is assumed that the particles seldom collide with one another. The particle energy per unit volume is related to the particle temperature through

$$E_p = \rho_p h_p + \tfrac{1}{2}\rho_p(u_p^2 + v_p^2)$$
$$h_p = \begin{cases} C_{ps} T_p, & \text{if } T < T_m \\ C_{ps} T_m - \chi \Delta h_f, & \text{if } T = T_m \\ C_{ps} T_m + C_{pl}(T_p - T_m) + \Delta h_f, & \text{if } T > T_m \end{cases} \tag{5}$$

where h_p is the particle enthalpy per unit mass and C_{ps} and C_{pl} are the specific heats of the solid and liquid particles, respectively. Δh_f is the latent heat of fusion, and T_m is the melting temperature of the particles. χ is the portion of the heat of fusion that the particles have when $T_p = T_m$. Note that for each particle size bin, we must solve Eq. (1).

The source terms represent the rate of momentum and energy transfer between the two phases. Additionally, the particles may cool through radiation; it is assumed that the gas does not absorb any of this emission. The rate of momentum transfer between the particle and gas phases may be found by considering the drag on a particle. In the x direction we have

$$m_p \frac{\mathrm{d}u_p}{\mathrm{d}t} = \frac{1}{2}\rho A_c C_D |u - u_p|(u - u_p) \tag{6}$$

where m_p and A_c are the mass and cross-sectional area of the particle. We can relate the drag coefficient, C_D, to the Stokes drag, through K_D, where

$$C_D = K_D C_{D\,\mathrm{Stokes}} = K_D(24/Re) \tag{7}$$

Re is the Reynolds number based on particle diameter and relative velocity

$$Re = \frac{2r_p \rho \sqrt{(u - u_p)^2 + (v - v_p)^2}}{\mu} \tag{8}$$

Thus, we can form the x-momentum source term as

$$w_{\rho u_p} = \rho_p \frac{\mathrm{d}u_p}{\mathrm{d}t} = \frac{9}{2}\frac{K_D \mu}{r_p^2}\frac{\rho_p}{\tilde{\rho}_p}\frac{|u - u_p|(u - u_p)}{\sqrt{(u - u_p)^2 + (v - v_p)^2}} \tag{9}$$

We obtain K_D from the work of Carlson and Hoglund[3] where they fit K_D as

$$K_D = \frac{(1 + 0.15Re^{0.687})[1 + \exp(-0.427/M^{4.63} - 3.0/Re^{0.88})]}{1 + (M/Re)[3.82 + 1.28\exp(-1.25Re/M)]} \tag{10}$$

where M is the Mach number based on the relative velocity. This expression is valid over the Mach and Reynolds numbers present in the simulations. The y-direction momentum exchange rate has a similar form as Eq. (9).

The energy source term for the particles has three components: 1) convective heat transfer to the gas, 2) radiative heat losses, and 3) energy input due to the work done by the drag forces. The convective heat transfer term may be derived in a similar fashion as the momentum exchange terms using an effective convective heat transfer coefficient. We obtain

$$\left.\frac{dE_p}{dt}\right|_{\text{conv}} = \frac{3}{Pr}\frac{\mu c_p K_H}{r_p^2}\frac{\rho_p}{\tilde{\rho}_p}(T - T_p) \tag{11}$$

where $\tilde{\rho}_p$ is the specific density of the particles, c_p is the specific heat at constant volume of the gas, and $K_H = k_{\text{eff}}/k$ has been developed in Ref. 3 as

$$K_H = \frac{1}{2}\left[\frac{2 + 0.459Re^{0.55}}{1 + 3.42(M/Re)(2 + 0.459Re^{0.55})}\right] \tag{12}$$

The radiative heat loss per unit mass is simply

$$\dot{Q}_{\text{rad}} = -(A\bar{\varepsilon}\sigma T_p^4/m_p) \tag{13}$$

where A and m_p are the particle surface area and mass. $\bar{\varepsilon} = \bar{\varepsilon}(r_p, T_p)$ is the wavelength-averaged blackbody emissivity.[2] σ is the Stefan-Boltzmann constant.

Therefore, adding these terms together, along with the terms due to the work done on the particles by the drag forces, we obtain

$$w_{E_p} = \left.\frac{dE_p}{dt}\right|_{\text{conv}} + \rho_p\dot{Q}_{\text{rad}} + w_{\rho u_p}u_p + w_{\rho v_p}v_p \tag{14}$$

From momentum and energy conservation, the gas-phase source terms are related to those of the particle phase. We have

$$\begin{aligned} w_{\rho u} &= -w_{\rho u_p}, \qquad w_{\rho v} = -w_{\rho v_p} \\ w_E &= -\left.\frac{dE_p}{dt}\right|_{\text{conv}} - w_{\rho u_p}u_p - w_{\rho v_p}v_p \end{aligned} \tag{15}$$

Numerical Method

Although the gas and particle phases have similar governing equations, they behave differently. The primary difference is that the particle motion is not affected by gradients of particle density, unlike a gas. Because of this difference, numerical methods that work well for gases, may not work for particle flows. However, some simple modifications to existing numerical schemes result in efficient and accurate methods for the simulation of particle flows. This scheme will be discussed in this section.

The gas-phase governing equations are solved using modified Steger-Warming flux-vector splitting[4-6] and an implicit Gauss-Seidel line-relaxation technique.[5,7] This method yields convergence to a steady state in a small number of iterations.[7]

To solve the particle flow governing equations, a much simpler method may be used. Let us consider the spatial differencing first. Note that the x-direction particle flux vector, F_p may be written as

$$\boldsymbol{F}_p = u_p\boldsymbol{U}_p \tag{16}$$

which implies that the mass, momentum, and energy are transported by the local velocity. Thus, we can use a true upwind (Steger-Warming[4]) scheme to evaluate the flux across the $i + \frac{1}{2}, j$ surface of a computational volume. We represent $\boldsymbol{F}_p$ as composed of forward and backward moving components

$$\begin{aligned} \boldsymbol{F}_{pi+1/2,j} &= \boldsymbol{F}^+_{pi+1/2,j} + \boldsymbol{F}^-_{pi+1/2,j} \\ \boldsymbol{F}^+_{pi+1/2,j} &= \tfrac{1}{2}(u_p + |u_p|)_{i,j}\boldsymbol{U}_{pi,j} \\ \boldsymbol{F}^-_{pi+1/2,j} &= \tfrac{1}{2}(u_p - |u_p|)_{i+1,j}\boldsymbol{U}_{pi+1,j} \end{aligned} \tag{17}$$

Then the x derivative of $\boldsymbol{F}_p$ is simply

$$\left.\frac{\partial \boldsymbol{F}_p}{\partial x}\right|_{i,j} = \frac{\boldsymbol{F}_{pi+1/2,j} - \boldsymbol{F}_{pi-1/2,j}}{\Delta x_{i,j}} \tag{18}$$

Now let us consider the time-integration of the governing equations. An implicit finite-difference representation of Eq. (1), where we have linearized the flux and the source vectors in time is

$$\delta U^n_{pi,j} + \Delta t\left(\frac{\partial}{\partial x}A_p\delta U_p + \frac{1}{y}\frac{\partial}{\partial y}yB_p\delta U_p - C_p\delta U_p\right)^n_{i,j}$$

$$= -\Delta t\left(\frac{\partial \boldsymbol{F}_p}{\partial x} + \frac{1}{y}\frac{\partial y\boldsymbol{G}_p}{\partial y} - \boldsymbol{W}_p\right)^n_{i,j} = \Delta U^n_{pi,j} \tag{19}$$

where $\delta U^n_p = U^{n+1}_p - U^n_p$, and A_p, B_p, and C_p are the Jacobians of $\boldsymbol{F}_p$, $\boldsymbol{G}_p$, and $\boldsymbol{W}_p$, respectively. Performing upwind differencing on the left-side of Eq. (19), yields, for example

$$\begin{aligned} \frac{\partial}{\partial x}(A_p\delta U_p)_{i,j} &= \frac{\partial}{\partial x}(A^+_p\delta U_p + A^-_p\delta U_p)_{i,j} \\ &= \frac{1}{\Delta x}(A^+_{pi,j}\delta U_{pi,j} - A^+_{pi-1,j}\delta U_{pi-1,j} \\ &\quad + A^-_{pi+1,j}\delta U_{pi+1,j} - A^-_{pi,j}\delta U_{pi,j}) \end{aligned} \tag{20}$$

Following the approach of Yoon and Jameson,[8,9] let us represent the Jacobians as

$$\begin{aligned} A^+_p &\simeq \tfrac{1}{2}[A_p + \rho(A_p)I] = \tfrac{1}{2}(A_p + u_pI) \\ A^-_p &\simeq \tfrac{1}{2}[A_p - \rho(A_p)I] = \tfrac{1}{2}(A_p - u_pI) \end{aligned} \tag{21}$$

where $\rho(A_p)$ is the spectral radius of A_p, which is u_p in this case. Then, we can approximate Eq. (20) as

$$\frac{\partial}{\partial x}(A_p\delta U_p)_{i,j} \simeq \frac{1}{\Delta x}(u_pI\delta U_p)_{i,j} \tag{22}$$

where we have neglected the off-diagonal terms in Eq. (20). It has been found that these terms may be destabilizing for the particle flow simulation, and as they have no contribution at the steady state, they may be neglected without loss of accuracy. Then, our finite-volume approximation to the particle-phase governing equations is

$$\left[\left(1 + \frac{\Delta t}{\partial x}u_p + \frac{\Delta t}{\Delta y}v_p\right)I - \Delta tC\right]\delta U^n_{pi,j} = \Delta U^n_{pi,j} \tag{23}$$

This expression is easy to evaluate except for the term involving C. If we approximate C as a diagonal matrix, we can

solve Eq. (23) with only a scalar inversion and obtain a steady-state solution with a small computational effort. Following the approach of Eberhardt et al.,[10,11] we can approximate C as

$$C \simeq -\beta_c \left| \frac{\partial w_{\rho u_p}}{\partial \rho_p u_p} \right| I \tag{24}$$

where β_c is an under-relaxation parameter, typically of order 0.01. This choice for the approximate C maintains diagonal dominance of Eq. (23) and results in rapid convergence for the problems of interest.

Line-of-Sight Calculations

The signal that the detector receives from particulate radiation may be computed from the simulated flow field. To do this, we must perform a line-of-sight calculation to determine the signal level from each part of the flow that the detector sees. The effective wavelength-dependent radiance observed by the instrument is

$$I_\lambda = \sum_j E_\lambda^j \Delta l_j \tag{25}$$

where E_λ^j is the wavelength-dependent emission from the particles at point j and Δl_j is the length of the jth volume element. E_λ^j is found by summing over all particle radii using the blackbody function and the temperature-dependent emissivity

$$E_\lambda^j = \sum_{i=1}^{n_{\text{radii}}} I_{bb}(\lambda, T_{ij}) \varepsilon_{ij}(\lambda) N_{ij} A_i$$
$$I_{bb}(\lambda, T_{ij}) = \frac{2c_1}{\lambda^5 (e^{c_2/\lambda T_{ij}} - 1)} \tag{26}$$

Where c_1 and c_2 are constants in the Planck spectral distribution of emission power,[12] T_{ij} is the ith particle temperature at point j, ε_{ij} is the emissivity,[2] N_{ij} is the particle number density, and A_i is the radiating area of particle type i

$$A_i = \pi r_{pi}^2 \tag{27}$$

where r_{pi} is the radius of particle i. To determine the flow characteristics that are needed to determine E_λ at each point in the line-of-sight calculation, we interpolate the flowfield data.

Rocket/Plume Flowfield Simulations

Four flowfields were simulated along the flight trajectory; two during the Antares II motor burn, and two during the Star-27 burn. These correspond to times-after-launch (TAL) of 161, 184, 245, and 271 s. The flight conditions are given in Table 1. The freestream gas was simulated using a molecular weight corresponding to air and a ratio of specific heats of 1.4. The characteristics of the gas exiting the nozzle depend on the rocket motor and will be discussed below. The particle flow was modeled using five particle size bins; the sizes and mass fractions for each bin are given in Table 2.

The nozzle flowfield was computed starting at the exit plane of the nozzle, with conditions obtained from the SPP code,[13] which are given in Table 3. A conical velocity distribution was assumed.

The flowfield was modeled using two grid blocks of size 170 × 190 and 60 × 190 for a total of 43,700 points. The first grid block is used to simulate the rocket hard-body flowfield and the near-nozzle flow. The second block was used to extend the solution downstream. The grid extends 75 m from the rocket motor exit plane and about 30 m from the centerline. Care was taken to align the grid with the nozzle exit angle so that as the particles leave the nozzle, their velocity is aligned along grid lines. It was found that this was necessary to reduce the numerical spreading of the particle plume. The grid was clustered near the hard-body surface and in the region of the plume-freestream interaction to reduce numerical errors.

Table 1 Trajectory conditions for flowfield simulations

TAL, s	Motor	Altitude	u_∞
161	Antares II	105.6	0.41
184	Antares II	109.6	1.97
245	Star-27	118.7	2.85
271	Star-27	114.0	4.59

Altitude in km and u_∞ in km/s.

Table 2 Particle sizes and mass fraction distribution used in simulations

Bin	$r_p(\mu)$	Mass fraction
1	0.5	0.10
2	1.5	0.38
3	2.5	0.32
4	3.5	0.15
5	4.5	0.05

Table 3 Nozzle exit-plane flow conditions used in flowfield simulations

	Antares II	Star-27
Gas		
u, km/s	2.651	2.934
ρ, kg/m^3	0.020915	0.010825
T, K	2139	1507
γ	1.2945	1.2917
M, kg/kmole	19.215	20.220
Particles		
ρ_p, kg/m^3	0.012428	0.004537
T_p, K	2320	2320
Nozzle angle	15.0 deg	17.2 deg

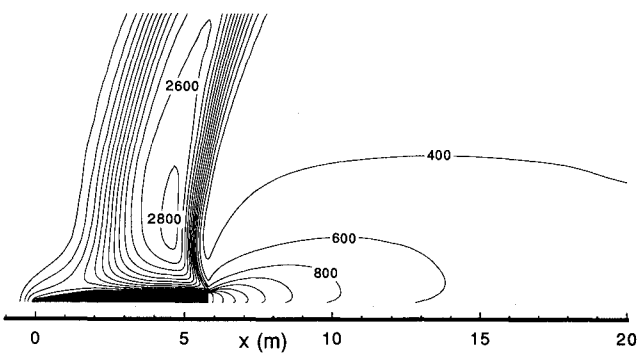

Fig. 2 Gas-phase temperature contours for the Antares II burn at TAL = 184 s, χ = 0.2. Contour levels in K. x and y axes have the same scale.

Several figures are presented to give a description of the computational results and the nature of the flowfield. These results are for TAL = 184 s; the Antares II motor at a freestream speed of 1.97 km/s and an altitude of 109.6 km. First, consider Fig. 2, which is a plot of the gas temperature contours for a portion of the simulated rocket/plume flow. We see the strong plume-induced shock which gives rise to the high-temperature region. This shock wave is very thick because of the low density of the freestream. At this altitude, the mean-free-path is slightly more than a meter, thus the shock thickness is reasonable. However, this indicates that the continuum formulation is suspect in this portion of the flow. Improvements to the modeling could be made by including slip wall boundary conditions and nonlinear constitutive relations. But, it is felt that these modifications would have little effect on the particle motion in the plume and on the present compar-

ison to the experiment. This may be seen if we consider Fig. 3, which is a plot of the logarithm of the plume gas density. We see that the plume flow is relatively dense and is confined by the flow that originates in the freestream. Thus, inaccuracies in the description of the low-density gas will not greatly affect the flow of the plume gas.

Now let us consider the particle flow. Figure 4 is a contour plot of the temperature of the 0.5-μ size particles for this case. We see that these small particles are swept far outboard due to their interaction with the gas. They pick up a large component of radial momentum in the near-nozzle region where the gas is dense. This carries them away from the nozzle centerline; their momentum is less affected farther away from the centerline because the gas is less dense, and therefore, there is less drag to alter the particle's velocity. If we consider the particle number density, plotted in Fig. 5, we see that the number of particles falls off rapidly with distance from the centerline. Beyond an angle of about 45 deg from the nozzle exit, there is less than one particle per cm^3. The large (4.5-μ) particles are swept less far outboard, as can be seen in Fig. 6, which is a contour plot of the number density. We see that

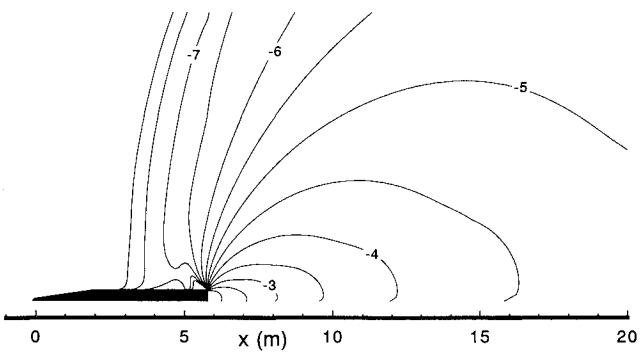

Fig. 3 Log_{10} of the density of the gas that originates in the rocket motor for the Antares II burn at TAL = 184 s, χ = 0.2. Contour levels in kg/m^3.

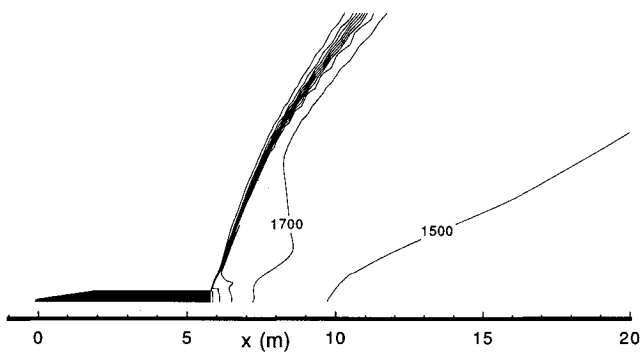

Fig. 4 0.5-μ Particle temperature contours for the Antares II burn at TAL = 184 s, χ = 0.2. Contour levels in K.

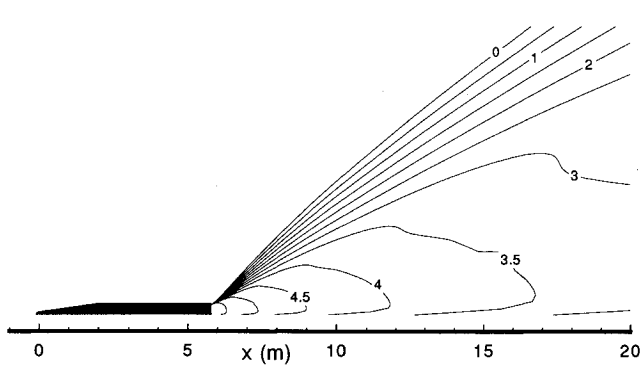

Fig. 5 Log_{10} of 0.5-μ particle number density contours for the Antares II burn at TAL = 184 s, χ = 0.2. Contour levels in cm^{-3}.

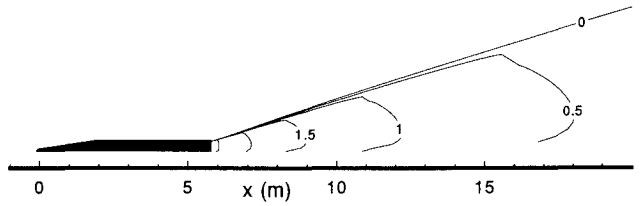

Fig. 6 Log_{10} of 4.5-μ particle number density contours for the Antares II burn at TAL = 184 s, χ = 0.2. Contour levels in cm^{-3}.

the particles are essentially confined to the region defined by the nozzle exit angle. Most of this region has a temperature of about 2200 K. The intermediate-sized particles have flowfields with characteristics between the two shown here.

Comparison to Data

The first comparison made to the experimental results is the spectral radiance detected by the photometers looking along the 4- and 25-deg lines of sight. These photometers have filters centered at 230 nm.[1]

Let us first consider the case discussed above (TAL = 184 s). Several computations were performed with a range of nozzle-exit particle enthalpies. We find that there is a nearly linear variation of the 4-deg viewing angle photometer signal with particle enthalpy as seen in Fig. 7. Thus, we can obtain any signal from the computation depending upon what enthalpy we give the particles as they exit the nozzle. The nozzle exit enthalpy obtained from the SPP code[13] gives results that are much larger than the experiment. With this numerical experimentation, we see that the enthalpy that the particles must have to produce the observed signal at 4 deg is about 3.4 MJ/kg. This enthalpy corresponds to the melting temperature of the particles with 20% of the latent heat of fusion (χ = 0.2). All subsequent calculations use this particle enthalpy, including those with the Star-27 motor. This method forces agreement with the data for this case, and because of the similarities of the flows, with the other cases also. This can be seen in Fig. 8, which is a plot of the experimental and computed photometer signals.

Now, let us consider the results that we obtain for the 25-deg viewing angle photometer. As can be seen in Fig. 8, the comparison is very poor. The computational results are at least four orders of magnitude lower than the experiment. There are at least three possible sources for this discrepancy. One is that there are too few particles making it far enough away from the centerline to be seen by the photometer; that is the momentum transfer model is inadequate. Another possible source of the difference is that the computed flowfields are wrong due to numerical inaccuracies. And finally, there may be another source of 230-nm radiation that is not modeled in the simulation.

The momentum transfer model discussed above is applicable over the range of conditions present in these simulations. Thus, we should have confidence that it is giving the correct results. The second concern has been addressed through mesh refinement and validation of the code. The size and spacing of the mesh was varied and it was found that the current mesh is sufficiently fine near the body that all relevant gradients are well resolved. The domain of the calculation was extended to determine if signal was coming from far downstream; this did not change the results. Extensive validation of the gas computation has been performed by comparison to experiments and other calculations and the particle flow algorithm has been tested on simple test problems where an exact solution is known. Thus, we have confidence in the numerical results. Therefore, there must be another source of radiation that is not being modeled.

Figures 9 and 10 show the comparison of computed spectral radiance with spectrometer data for scans obtained during the Antares motor burn at a scan start time of 184 s and during the Star-27 motor burn for a scan start time of 271 s. The

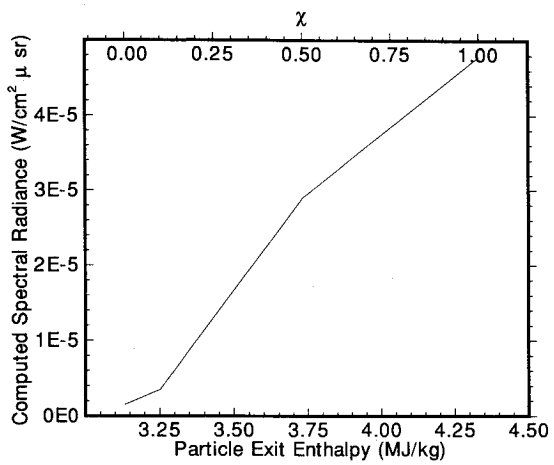

Fig. 7 Variation of computed 230 nm spectral radiance on 4-deg line-of-sight with particle exit enthalpy for the TAL = 184 s case.

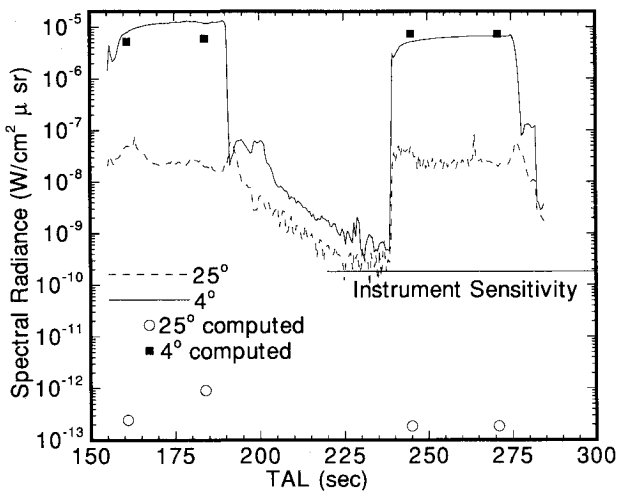

Fig. 8 Comparison of computed and experimental 230-nm spectral radiance for 4- and 25-deg photometers.

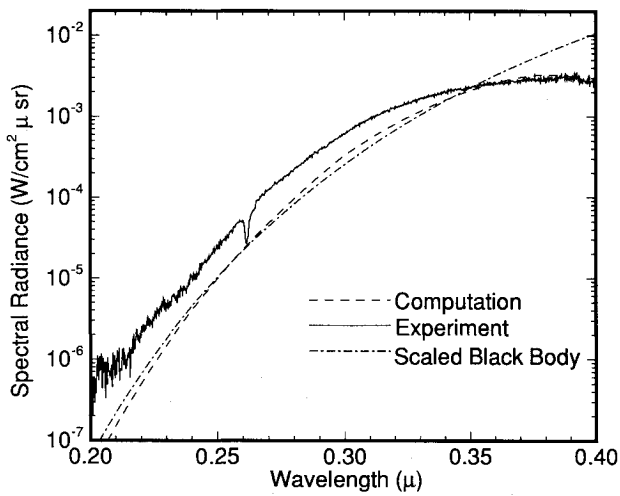

Fig. 9 Comparison of computed and experimental spectrum along the 4-deg line-of-sight for the TAL = 184 s case.

agreement between theory and experiment in terms of absolute magnitude as well as wavelength dependence is good. For wavelengths less than 0.3 μ the spectral data for the TAL = 184 s case can be fit by a blackbody function at a temperature of 2320 K scaled by a factor of 0.05, which is plotted in Fig. 10. Two-color wavelength fits to the spectrometer data produce a temperature of 2320 K which is consistent with the phase transition of Al_2O_3. This scaling demonstrates that the

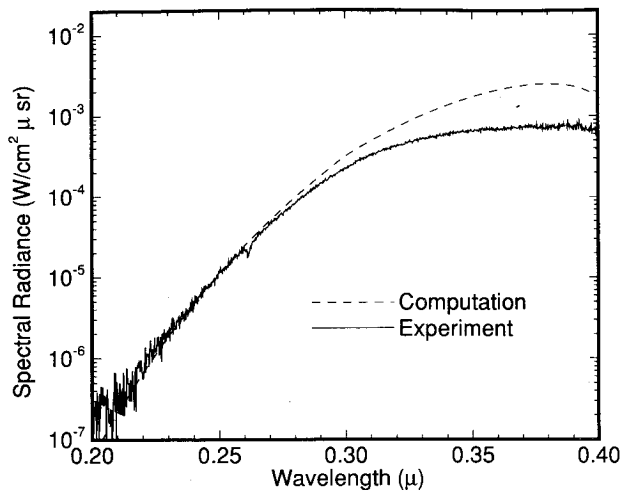

Fig. 10 Comparison of computed and experimental spectrum along the 4-deg line-of-sight for the TAL = 271 s case.

particulate emission is optically thin. The deviation in both computation and experiment from the blackbody at wavelengths longer than 0.3 μ is due to the change in particle emissivity at longer wavelengths.[2] Both computation and data show a maximum at 0.38 μ. In the absence of data at wavelengths greater than 0.4 μ, it was felt that the computational overprediction at wavelengths greater than 0.35 μ could not be meaningfully addressed by parameterization of particle emissivity or size.

As shown in Ref. 1, the spectrometer clearly records the CO Cameron bands along the 4-deg line-of-sight during the time after Antares and Star motor burnout. Examination of spectra obtained during the motor burns also shows evidence of molecular band structure at wavelengths shorter than 0.3 μ. For example, the absorption feature observed at 0.26 μ in Figs. 9 and 10 has been attributed to cool AlCl combustion products in AEDC chamber measurements.[14] The absorption band at 0.2637 μ was found to be present in all spectra. Although structure observed in the experimental spectra is suggestive of molecular band emission, definitive confirmation is probably not possible for these flight data. Small temperature fluctuations observed during the Antares motor burn can produce intensity variations in the UV emission on time scales comparable to the 1 s spectrometer scan time. Measurements taken on future flights that employ faster scan rates and obtain spectral data at other locations in the flow would help to resolve questions about the relative contribution of UV particulate and molecular radiation. Since we do not predict any signal for the far-field photometers with particulates as the sole radiation source, an estimate of the potential amount of radiation due to molecular emission is useful.

We can estimate the radiance contribution due to the gas assuming that CO Cameron band emission is observed during the motor burns. The CO Cameron band molecular radiation intensity along a line-of-sight is given as

$$I_{CO} = \sum_j \frac{\Delta x_j}{2} \frac{\int T_f(\lambda)\lambda I_j^{n',n''}(\lambda)\, d\lambda}{\int T_f(\lambda)\lambda\, d\lambda} \tag{28}$$

where T_f is the photometer filter function and $I_j^{n',n''}$ is the emission from the initial molecular state, $n' = |n', v', J'\rangle$, to the final state, $n'' = |n'', v'', J''\rangle$, at the jth grid location which is given as

$$I_j^{n',n''} = \frac{ch\nu_{n',n''}}{2\pi} P_\lambda A_{v',v''}^{n',n''} \frac{N_{CO_j}}{Q} S_{J',J''} \times \exp[-hc/kT_{exj}(T_{n'} + G_{v'} + F_{J'})] \tag{29}$$

Indices n, v, and J represent the electronic, vibrational, and rotational quantum levels of the molecule; T_{ex_j} is the governing excitation temperature for the excited state, n'; k is the Boltzmann constant; N_{CO_j} is the total number of CO molecules; Q represents the total molecular partition function; $A^{n',n''}_{v',v''}$ is the Einstein A coefficient for spontaneous emission; and P_λ is the molecular line shape (assumed Voight). The remaining symbols in Eq. (29) follow the convention given in Herzberg.[15] Average values for the electronic energy term value, $T_{n'}$, and the radiative life time of the Cameron state are 48,600 cm^{-1} and 9.5×10^{-3} s, respectively.

The CO Cameron band is a spin forbidden transition from the $a^3\Pi$ to the $X^1\Sigma^+$ state,[15] which accounts for its long radiative lifetime. We have used the spectral emission model of Bernstein[16] to evaluate Eq. (29) at each grid location j. This model incorporates the branching ratios and transition probabilities obtained by Conway[17] and James[18] and the line intensity factors, $S_{J',J''}$, given by Kovacs.[19]

The temperature that characterizes the excited state population of CO, T_{ex_j}, is the major uncertainty in the modeling. There are three possible mechanisms for the production of CO, all leading to different excitation temperatures. First, the CO that is produced in the motor could be equilibrated to the local gas conditions; this would result in an excitation temperature equal to the local gas temperature. Secondly, there could be a production of excited CO due to thermochemical excitation of the plume gas as it encounters the freestream gas. This would produce CO at a high temperature characteristic of the temperature within the plume shock (see Fig. 2). Thirdly, the CO produced within the motor could be convected downstream so quickly that the internal energy is frozen near the throat conditions. This would produce an excitation temperature similar to the throat conditions. While a definitive calculation of the second and third possibilities is beyond the scope of this article, preliminary arguments can be made based on the methodology developed here and analyses of the 184-s TAL photometer data and spectral data after Antares motor burnout. We approximate N_{CO_j} by the product of the nozzle exit CO mole fraction and the local plume gas number density.

Use of the local gas temperature in Eq. (29) to compute the 25-deg photometer radiance yields 2.5×10^{-13} W/cm^2 μsr, which is clearly incorrect since it is below the detection limit of the instrument.

Since the radiative lifetime of the CO Cameron bands is sufficiently long that the gas travels an appreciable distance before it is quenched, a governing temperature representative of throat conditions was considered. If the Antares throat temperature of 3355 K is assumed to be characteristic of the conditions in Eq. (29), we obtain a value of 5.4×10^{-7} W/cm^2 μsr for the 25-deg viewing angle photometer as compared with the observed value of 2.0×10^{-8}. This simple approach overpredicts the signal, but a decrease in that temperature of 300 K reduces the computed value to 3.9×10^{-8} W/cm^2 μsr. We would expect a more accurate calculation of the excitation temperature that incorporates quenching of the $a^3\Pi$ state population to give an effective excitation temperature lower than the throat temperature. Evaluation of Eq. (28) along the 4-deg line-of-sight with the throat temperature gives a radiance of 5.1×10^{-6} W/cm^2 μsr, or about 50% of the measured signal; this may account for noncontinuum features in the gray-body spectrum shown in Fig. 9.

We can also test the assumption implicit in Eq. (29), i.e., the electronic excitation, rotational, and vibrational temperatures are equal, by considering the spectral data from the 4-deg viewing angle. We would expect these temperatures to be equilibrated if the source of the excitation is due to combustion in the chamber rather than the plume shock-induced chemistry. The latter would be expected to produce vibrational temperatures higher than 3000 K and out of equilibrium with the rotational and electronic excitation temperatures. The observed spectral shape and peak height ratios of the CO Cameron band spectral data gives us information regarding the upper electronic state vibrational and rotational temperatures. Synthetic spectra were computed for vibrational temperatures between 2000–6000 K in increments of 1000 K, and rotational temperatures from 1000 to 3000 K. The best peak shapes and height ratios were obtained with rotational and vibrational temperatures of about 3000 K, characteristic of the throat temperature. Therefore, based on the spectra at 4 deg, we find an upper state distribution characterized by a single temperature, indicating that the source of the radiation is the rocket motor, not the plume shock.

Conclusions

A computational fluid dynamics algorithm has been developed to simulate the interaction of a hypersonic freestream with the exhaust plume of a solid rocket motor. The method treats the gas as composed of two different types: 1) gas that originates in the freestream, and 2) gas that comes from the rocket exhaust. This allows the different characteristics of these two gases to be simulated. The particles are placed in five different bins depending on their size. Mass, momentum, and energy equations are solved for each bin allowing different sized particles to migrate and change temperature according to their characteristics. Finite-rate momentum and energy exchange models are used to model the interaction of the two phases. The particles are also cooled by radiation which is not absorbed by the gas phase.

The computational method has been applied to four different conditions along the trajectory of the bow shock ultraviolet 2 flight experiment. With an appropriate choice of the enthalpy of the particles as they leave the rocket motor nozzle, we obtain very good agreement along the 4-deg viewing angle. However, we underpredict the signal along the 25-deg line-of-sight by at least four orders of magnitude. Approximate calculations have been performed to assess the importance of CO Cameron bands as a source of UV radiation. This shows that if we populate the excited states of CO using the nozzle throat temperature, we obtain a signal consistent with that seen by the spectrometer along the 4-deg line-of-sight. At 25 deg, this approach yields too much signal, but a more accurate calculation would give better agreement. This suggests that molecular band emission from a long-lived electronic state of a major gaseous combustion product may be a source of UV radiance in the plume far-field.

The method shows promise for continued development as a tool for the analysis of high-altitude plume signatures. Further work is required in the development and testing of the momentum and energy exchange models and in the incorporation of a realistic chemistry model.

Acknowledgments

This research was supported by Strategic Defense Initiative Organization/IST managed by the Army Research Office under Contract MDA903-89-C-0003. We would like to acknowledge the many useful technical discussions that we have had with Carol Christou, John Brandenburg, and Larry Bernstein.

References

[1]Erdman, P. W., Zipf, E., Espy, P., Howlett, C., Levin, D. A., and Candler, G. V., "In-Situ Measurements of UV and VUV Radiation from a Rocket Plume and Re-Entry Bow Shock," AIAA Paper 92-0124, Jan. 1992.

[2]Freeman, G. N., Crow, D. R., Malkmus, W., Wilson, K. H., Thomas, P. D., and Elgin, J. B., "Composite High Altitude Radiation Model (CHARM)," Vol. 1 Code Development, Photon Research Associates, Air Force Astronautics Lab. TR-87-019, La Jolla, CA, Sept. 1987.

[3]Carlson, D. J., and Hoglund, R. F., "Particle Drag and Heat Transfer in Rocket Nozzles," *AIAA Journal*, Vol. 2, No. 11, 1964, pp. 1980–1984.

[4]Steger, J., and Warming, R. F., "Flux Vector Splitting of the Inviscid Gasdynamics Equations with Application to Finite Differ-

ence Methods," NASA TM-78605, June 1979.

[5]MacCormack, R. W., and Candler, G. V., "The Solution of the Navier-Stokes Equations Using Gauss-Seidel Line Relaxation," *Computers and Fluids*, Vol. 17, No. 1, 1989, pp. 135–150.

[6]Van der Vegt, J. J. W., "Assessment of Flux Vector Splitting for Viscous Compressible Flows," AIAA Paper 91-0242, Jan. 1991.

[7]MacCormack, R. W., "Current Status of the Numerical Solutions of the Navier-Stokes Equations," AIAA Paper 85-0032, Jan. 1985.

[8]Yoon, S., and Jameson, A., "An LU-SSOR Scheme for the Euler and Navier-Stokes Equations," AIAA Paper 87-0600, Jan. 1987.

[9]Yoon, S., and Kwak, D., "An Implicit Three-Dimensional Navier-Stokes Solver for Compressible Flow," AIAA Paper 91-1555-CP, June 1991.

[10]Eberhardt, S., and Imlay, S., "A Diagonal Implicit Scheme for Computing Flows with Finite-Rate Chemistry," AIAA Paper 90-1577, June 1990.

[11]Imlay, S., Roberts, D., Soestrisno, M., and Eberhardt, S., "Nonequilibrium Thermo-Chemical Calculations Using Diagonal Implicit Scheme," AIAA Paper 91-0468, Jan. 1991.

[12]Vincenti, W. G., and Kruger, C. H., Jr., *Introduction to Physical Gas Dynamics*, Krieger Publishing, Malabar, FL, 1965.

[13]Nickerson, G. R., Coates, D. E., Dang, A. L., Dunn, S. S., Berker, D. R., Hermsen, R. L., and Lamberty, J. T., "The Solid Propellant Motor Performance Prediction Computer Program (SPP)," Air Force Astronautics Lab. TR-87-078, Dec. 1987.

[14]Beale, K. S., McGregor, W. K., Frederick, R. A., Reed, R. A., and Roberts, D. W., "Diagnostic Measurements on an Aluminized Propellant Plume During Spin and Nonspin Testing," Arnold Engineering Development Center TR-90-28, Feb. 1991.

[15]Herzberg, G., *Molecular Spectra and Molecular Structure, I. Spectra of Diatomic Molecules*, Van Nostrand Reinhold, New York, 1950.

[16]Berk, A., Bernstein, L., Richtsmeier, S., Cox, J., and Slack, M., "UV-VIS NLTE Plume Spectral Emission Model," *Proceedings of InfraRed Information Symposia (IRIS) Targets, Backgrounds, and Discrimination*, Vol. I, Jan. 1990, p. 69.

[17]Conway, R., "Spectroscopy of the Cameron Bands in the Mars Airglow," *Journal of Geophysical Research*, Vol. 86, No. A6, 1981, pp. 4767–4775.

[18]James, T., "Transition Moments, Franck-Condon Factors, and Lifetimes of Forbidden Transitions. Calculation of the Intensity of the Cameron System of CO," *Journal of Chemical Physics*, Vol. 55, No. 8, 1971, pp. 4118–4124.

[19]Kovacs, I., *Rotational Structure in the Spectra of Diatomic Molecules*, Elsevier, New York, 1969.